



# Hydrodynamic Model Description Carradale North & Carradale (South) CAR/L/1131788 & CAR/L/1078064

December 2023

Mowi Scotland	OFFICE	PHONE	FAX
	Mowi, Farms Office, Glen Nevis Business Park PH33 6RX Fort William		-
	POSTAL	MAIL	
	Mowi, Farms Office, Glen Nevis Business Park PH33 6RX Fort William	environment@mowi.com	
		WEB	
		<a href="http://mowiscotland.co.uk">http://mowiscotland.co.uk</a>	

**CONTENTS**

	Page
<b>1. MODEL DESCRIPTION</b>	<b>3</b>
<b>2. CONFIGURATION AND BOUNDARY FORCING FOR CARRADALE</b>	<b>4</b>
<b>3. MODEL CALIBRATION AND VALIDATION</b>	<b>7</b>
<b>3.1 Calibration: September – December 2016, ID119</b>	<b>8</b>
<b>3.2 Validation: August – October 2017, ID182</b>	<b>11</b>
<b>4. MODELLED FLOW FIELDS (ID119)</b>	<b>14</b>
<b>5. REFERENCES AND BIBLIOGRAPHY</b>	<b>14</b>

## LIST OF FIGURES

<i>Figure 1. The modified Firth of Clyde mesh and domain of the modelling study (Marine Scotland, 2019)</i>	5
<i>Figure 2. The unstructured mesh around the Carradale sites in the modified model grid, with the proposed cage locations indicated (○).</i>	6
<i>Figure 3. Model water depths (m) in the area around the Carradale sites. The pen locations indicated (○).</i>	7
<i>Figure 4. The current pen layouts at both Carradale North and Carradale (South). Current meter positions are shown by the black triangles</i>	8
<i>Figure 5. Comparison between observed and modelled sea surface height from September – December 2016 (ADCP deployment ID119) using model parameter values from Table 1. Both the full record (left) and a subset of 15 days (right) are shown. Observed data are in blue, model results in red.</i>	9
<i>Figure 6. Comparison between observed and modelled East (top) and North (bottom) components of velocity at the ADCP location for 15 days in September - October 2018 (ID119). Observed data are in blue, model results in red.</i>	10
<i>Figure 7. Scatter plot of observed and modelled velocity at the ADCP location from September – December 2016 (ID119). Observed data are in blue, model results in red.</i>	10
<i>Figure 8. Histograms of observed and modelled speed (top) and direction (bottom) at the ADCP location from September – December 2016 (ID119). Observed data are in blue, model results in red.</i>	11
<i>Figure 9. Comparison between observed and modelled sea surface height from August– October 2017 (ADCP deployment ID182) using model parameter values from Table 1. Both the full record (left) and a subset of 15 days (right) are shown. Observed data are in blue, model results in red.</i>	12
<i>Figure 10. Comparison between observed and modelled East (top) and North (bottom) components of velocity at the ADCP location for 15 days in August – October 2017 (ID182). Observed data are in blue, model results in red.</i>	12
<i>Figure 11. Scatter plot of observed and modelled velocity at the ADCP location from August – October 2017 (ID182). Observed data are in blue, model results in red.</i>	13
<i>Figure 12. Histograms of observed and modelled current speed (top) and direction (bottom) at the ADCP location from August – October 2017 (ID182). Observed data are in blue, model results in red.</i>	13

Figure 17. Modelled flood (left) and ebb (right) surface current vectors during spring tides.

For clarity, only every 10<sup>th</sup> vector is shown.

14

### **LIST OF TABLES**

Table 1. Parameter values chosen for the RiCOM model during the calibration simulations.. 8

Table 2. Model performance statistics for sea surface height (SSH) and East and North velocity at the ADCP location from September – December 2016 (ID119). ..... 9

Table 3. Model performance statistics for sea surface height (SSH) and East and North velocity at the ADCP location from August – October 2017 (ID182). .....11

## 1. Model Description

The hydrodynamic model used in the Carradale Azamethiphos Dispersion Modelling (Mowi Scotland Ltd., 2023) was RiCOM (River and Coastal Ocean Model), a general-purpose hydrodynamics and transport model, which solves the standard Reynolds-averaged Navier-Stokes equation (RANS) and the incompressibility condition, applying the hydrostatic and Boussinesq approximations. It has been tested on a variety of benchmarks against both analytical and experimental data sets (e.g. Walters & Casulli 1998; Walters 2005a, b). The model has been previously used to investigate the inundation risk from tsunamis and storm surge on the New Zealand coastline (Walters 2005a; Gillibrand et al. 2011; Lane et al. 2011), to study tidal currents in high energy tidal environments (Walters et al. 2010) and, more recently, to study tidal energy resource (Plew & Stevens 2013; Walters et al. 2013; Walters 2016) and the effects of energy extraction on the ambient environment (McIlvenny et al. 2016; Gillibrand et al. 2016).

The basic equations considered here are the three-dimensional (3D) shallow water equations, derived from the Reynolds-averaged Navier-Stokes equations by using the hydrostatic assumption and the Boussinesq approximation. The continuity equation for incompressible flows is:

$$\nabla \cdot \mathbf{u} + \frac{\partial w}{\partial z} = 0 \quad (1)$$

where  $\mathbf{u}(x,y,z,t)$  is the horizontal velocity vector,  $w(x,y,z,t)$  is the vertical velocity,  $\nabla$  is the horizontal gradient operator, and  $z$  is the vertical coordinate. The momentum equation in non-conservative form is given by:

$$\frac{D\mathbf{u}}{Dt} + f\hat{z} \times \mathbf{u} + \frac{1}{\rho_0} \nabla p - \frac{\partial}{\partial z} \left( A_V \frac{\partial \mathbf{u}}{\partial z} \right) - \nabla \cdot (A_h \nabla \mathbf{u}) + \mathbf{F} = 0 \quad (2)$$

where  $t$  is time;  $f(x,y)$  is the Coriolis parameter;  $\hat{z}$  is the upward unit vector;  $p(x,y,z,t)$  is pressure;  $\rho_0$  is a reference density;  $A_V(x,y,z,t)$  and  $A_h(x,y,z,t)$  are the vertical and horizontal eddy viscosities respectively;  $\mathbf{F}$  represents body forces including form drag from obstacles in the flow; and  $x, y$  are the horizontal coordinates aligned to the east and north respectively.

The free surface equation is formed by vertically integrating the continuity equation and applying the kinematic free surface and bottom boundary conditions:

$$\frac{\partial \eta}{\partial t} - \nabla \cdot \left( \int_{-H}^{\eta} \mathbf{u} dz \right) = 0 \quad (3)$$

where  $H$  is the water depth relative to the mean level of the sea.

The model can be run in two- or three-dimensional mode. Frictional stress,  $\tau_b$ , is applied at the seabed as a quadratic function of velocity:

$$\tau_b = \rho C_D U_b |U_b| \quad (4)$$

where  $\rho = 1025 \text{ kg m}^{-3}$  is the water density. The velocity,  $U_b$ , is either the velocity at the lowest sigma layer if the model is run in 3D or the depth-averaged velocity if run in 2D. The drag coefficient,  $C_D$ , can be either a constant or calculated from the bed roughness lengthscale,  $z_0$ , using:

$$C_D = \left( \frac{\kappa}{\ln((z_b + z_0)/z_0)} \right)^2 \quad (5)$$

where  $\kappa=0.4$  is von Karman's constant, and  $z_b$  is the height above the bed of the lowest velocity point.

Wind forcing was applied as a surface stress calculated from hourly wind speed and direction. Wind stress was calculated from the wind velocity by a standard quadratic relation:

$$\tau_x = \rho_a C_S u W \quad (6a)$$

$$\tau_y = \rho_a C_S v W \quad (6b)$$

where  $(u,v)$  are the East and North components of wind velocity respectively,  $W$  is the wind speed ( $W = [u^2 + v^2]^{1/2}$ ),  $\rho_a$  is the density of air, and the surface drag coefficient  $C_S$  is calculated following Wu (1982) or Large and Pond (1981).

The equations are discretized on an unstructured grid of triangular elements which permits greater resolution of complex coastlines. The momentum and free surface equations are solved using semi-implicit techniques to optimize solution time and avoid the CFL stability constraint (Walters 2016). The material derivative in (2) is discretized using semi-Lagrangian methods to remove stability constraints on advection (Casulli, 1987; Walters et al. 2008). The Coriolis term is solved using a 3<sup>rd</sup> order Adams-Bashforth method (Walters et al. 2009). Full details of the model discretization and solution methods can be found in Walters et al. (2013) and Walters (2016). The solution methods provide a fast, accurate and robust code that runs efficiently on multi-core desktop workstations with shared memory using OpenMP. Full details of the model discretization and solution methods, including the basis of the application to tidal energy, are given by Walters et al. (2013) and Walters (2016).

## 2. Configuration and Boundary Forcing for Carradale

The unstructured mesh used in the modelling (Figure 1) was adapted from The Firth of Clyde sub-model mesh of the Scottish Shelf Model (Marine Scotland, 2019). The model resolution was enhanced in the Kilbrannan Sound region, particularly around both the Mowi sites, Carradale North and Carradale (South) (Figure 2). The spatial resolution of the model varied from 18 m in some inshore waters and round the farm pens to 3 km along the open boundary. The model consisted of 68,390 nodes and 130,139 triangular elements. The model was run in 2D mode. Model bathymetry was also taken from The Firth of Clyde model and local multibeam bathymetry in Kilbrannan Sound.

The model is forced at the outer boundaries by 12 tidal constituents ( $M_2$ ,  $S_2$ ,  $N_2$ ,  $K_2$ ,  $O_1$ ,  $K_1$ ,  $P_1$ ,  $Q_1$ ,  $M_4$ ,  $MU_2$ ,  $L_2$ ,  $MS_4$ ) which were derived from tidal analysis (Pawlowicz et al., 2002) of the sea surface elevations at the closest nodes from the Scottish Shelf Model climatology (Marine Scotland, 2016). Spatially- and temporally-varying wind speed and direction data are taken from the ERA5 global reanalysis dataset (ECMWF, 2021) for the required simulation periods.

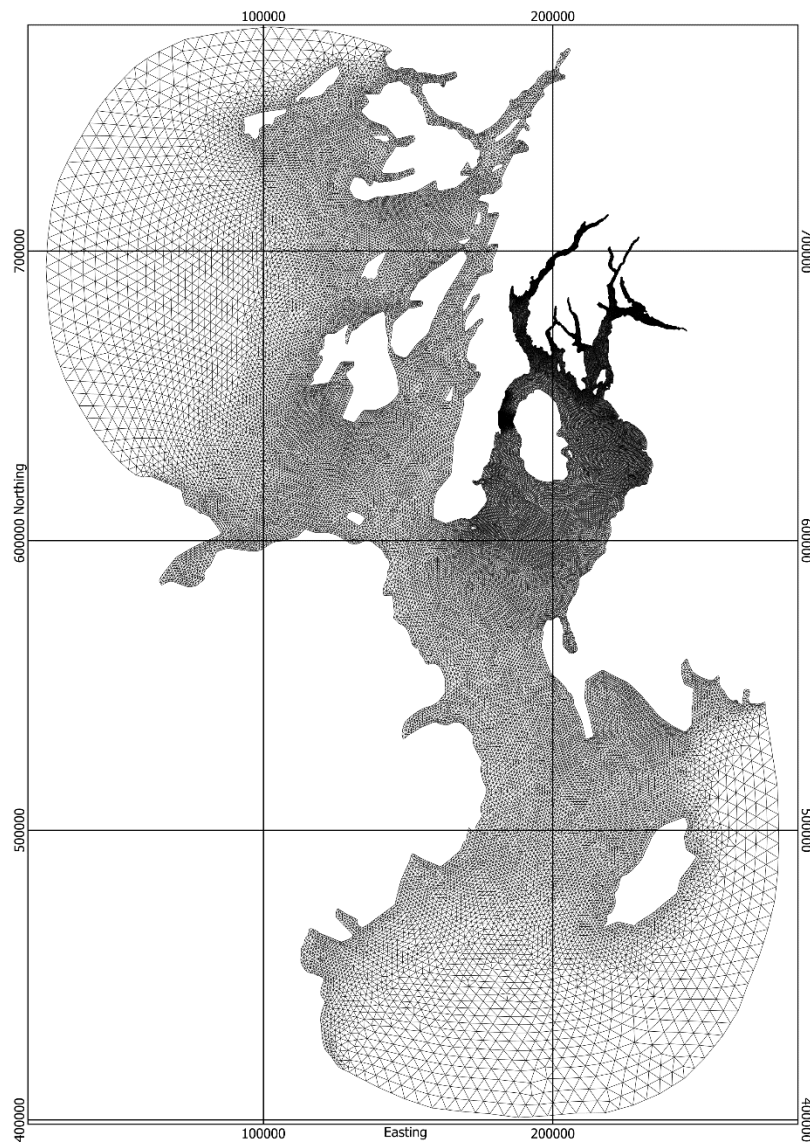


Figure 1. The modified Firth of Clyde mesh and domain of the modelling study (Marine Scotland, 2019)

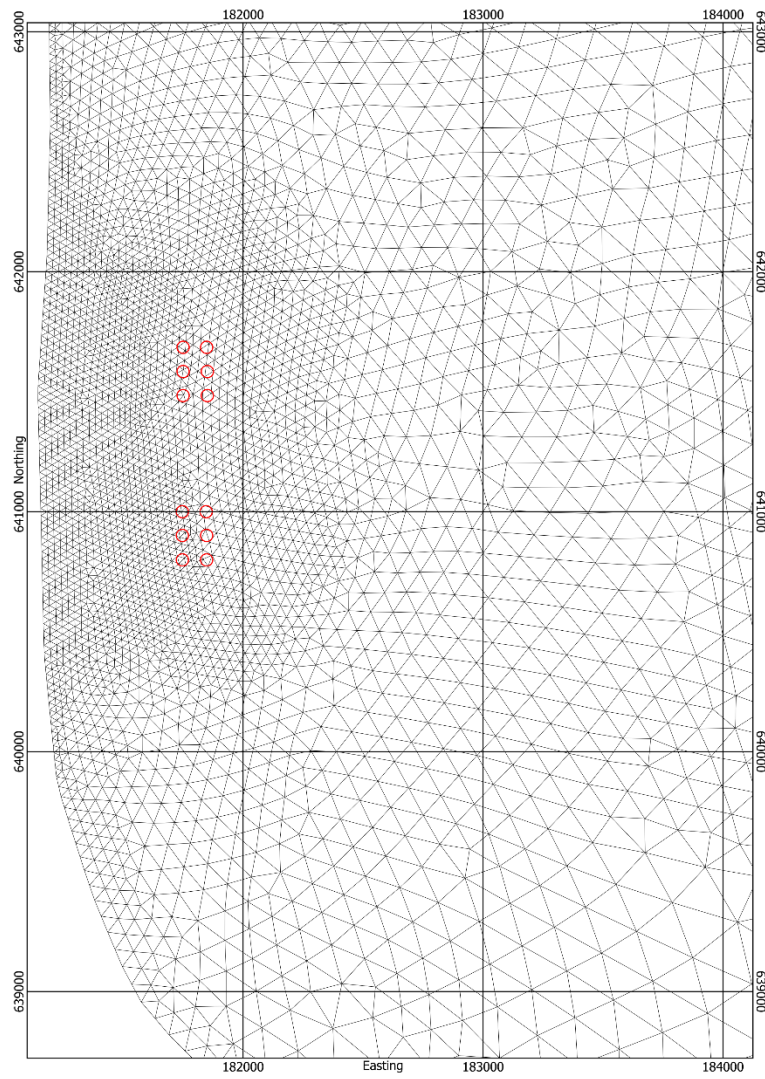


Figure 2. The unstructured mesh around the Carradale sites in the modified model grid, with the proposed cage locations indicated (○).



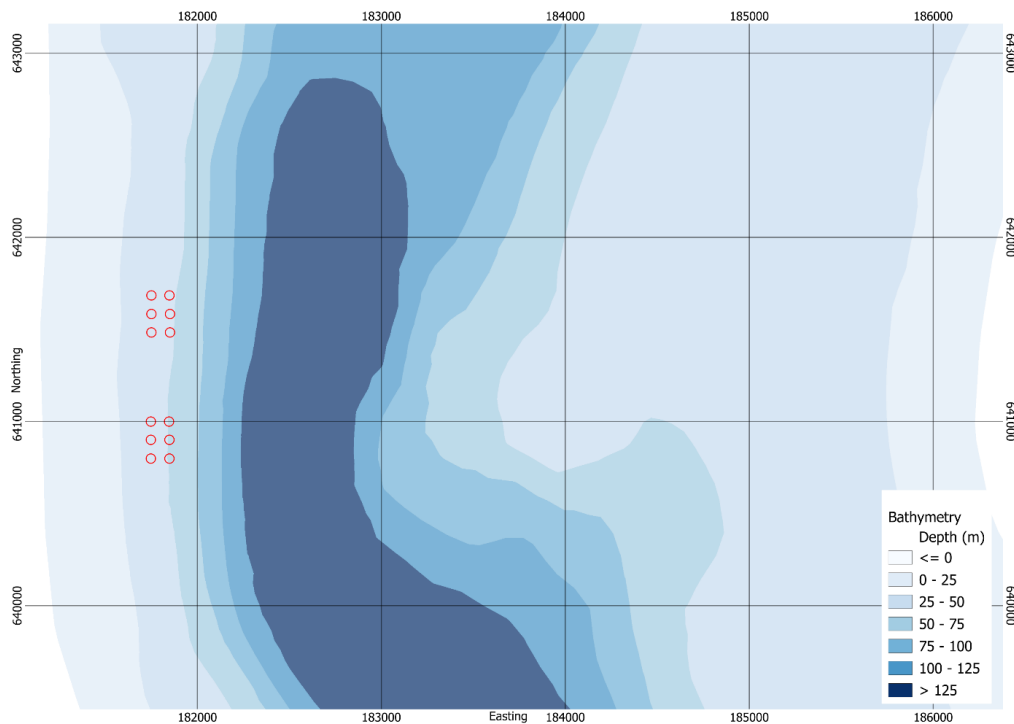


Figure 3. Model water depths (m) in the area around the Carradale sites. The pen locations indicated (○).

### 3. Model Calibration and Validation

The RiCOM model has previously been calibrated against sea level and current meter data from the north of Scotland (Gillibrand et al. 2016). For the current study, the model was further calibrated against hydrographic data collected in the region of the Carradale (South) farm site in 2016. The data are described in the relevant hydrographic reports. In September 2016, an Acoustic Doppler Current Profiler (ADCP) was deployed close to the farm site (Figure 4) until December 2016 (ID119). In August 2017, another ADCP was deployed close to Carradale North (Figure 4) until October 2017 (ID182). In all, 122 days of current data were used in this application. ADCP deployments provided both current velocity and seabed pressure data, which were used to calibrate and validate modelled velocity and sea surface height. The model was calibrated initially against data from February – May 2016 (ID119), then validated against data from the second deployment period, ID182.

For each simulation, the model was “spun-up” for three days with boundary forcing ramped up from zero over a period of 48 hours. The model state at the end of the 72-hour spin-up period was stored, and the main simulations “hot-started” from this state.

The following main simulations were performed, corresponding with the dates of the ADCP deployments:

- (i) Calibration: 30<sup>th</sup> September – 12<sup>th</sup> December 2016 (ID119, Carradale (South))
- (ii) Validation: 8<sup>th</sup> August – 6<sup>th</sup> October 2017 (ID182, Carradale North)

[Note that the dates above refer to the main simulations and that the spin-up simulations ran for three days prior to the start dates given above.]

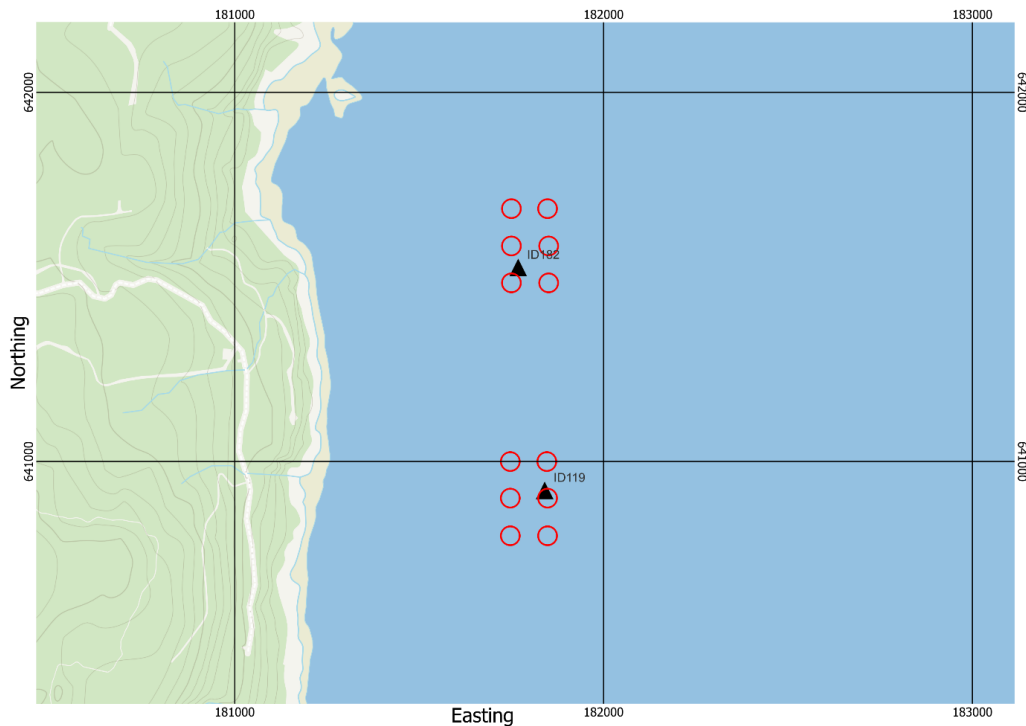


Figure 4. The current pen layouts at both Carradale North and Carradale (South). Current meter positions are shown by the black triangles

Model performance is assessed using three metrics: the mean absolute error (MAE), the root-mean-square error (RMSE) and the model skill ( $d_2$ ). The first two are standard measures of model accuracy; the third,  $d_2$ , is taken from Willmott et al. (1985) and lies in the range  $0 \leq d_2 \leq 1$ , with  $d_2 = 0$  implying zero model skill and  $d_2 = 1$  indicating perfect skill.

### 3.1 Calibration: September – December 2016, ID119

The calibration used observed depth and current velocity from the ADCP location to compare with modelled sea surface height (SSH) and velocity (ADCP deployment ID119). The model was calibrated by varying the value of the drag coefficient,  $C_D$ , in Equation 4, which determines the frictional effect of the seabed on the flow. Simulations were performed with a range of values of  $C_D$ , varying over the range  $0.002 \leq C_D \leq 0.2$ . After a number of simulations, a final parameter set was selected (Table 1).

Table 1. Parameter values chosen for the RiCOM model during the calibration simulations.

Parameter Description	Value
Drag coefficient, $C_D$	0.005
Number of vertical levels	1
Model time step (s)	36

The results of the calibration exercise are presented in Figure 5 – Figure 8 and Table 2. At the ADCP location, the sea surface height was reasonably accurately modelled, with model skill of 0.96. The mean absolute error (MAE) and root-mean-square error (RMSE) values of 0.28 m and 0.34m are about 7% and 8.5% of the spring tide range (ca. 4 m) respectively.

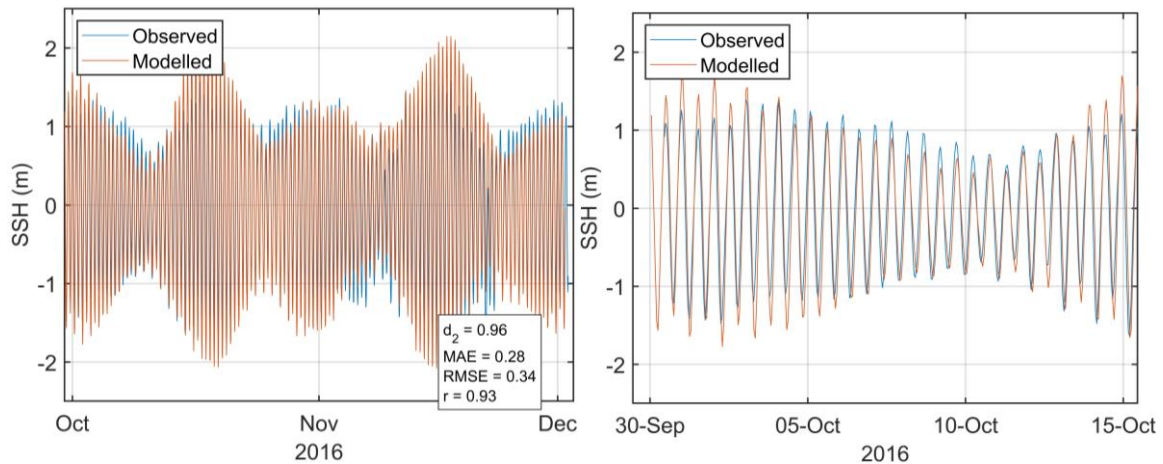


Figure 5. Comparison between observed and modelled sea surface height from September – December 2016 (ADCP deployment ID119) using model parameter values from Table 1. Both the full record (left) and a subset of 15 days (right) are shown. Observed data are in blue, model results in red.

For the calibration period, the model skill scores were 0.14 and 0.93 for the East and North components of velocity respectively. RMSE values were 0.03 and 0.08 respectively (Table 2). The scatter plots and histograms demonstrate that the modelled current had broadly the same magnitude and direction characteristics as the observed data (Figure 7 and Figure 8). The low skill score for the East component is due to the weak lateral flows in Kilbrannan Sound – the flow at the site is predominantly orientated along the North – South axis (see also Figure 17), for which there is very good agreement.

Table 2. Model performance statistics for sea surface height (SSH) and East and North velocity at the ADCP location from September – December 2016 (ID119).

	SSH	East	North
Model skill, $d_2$	0.96	0.14	0.93
Mean Absolute Error (MAE)	0.28 m	0.03 m s <sup>-1</sup>	0.06 m s <sup>-1</sup>
Root-Mean-Square Error (RMSE)	0.34 m	0.03 m s <sup>-1</sup>	0.08 m s <sup>-1</sup>

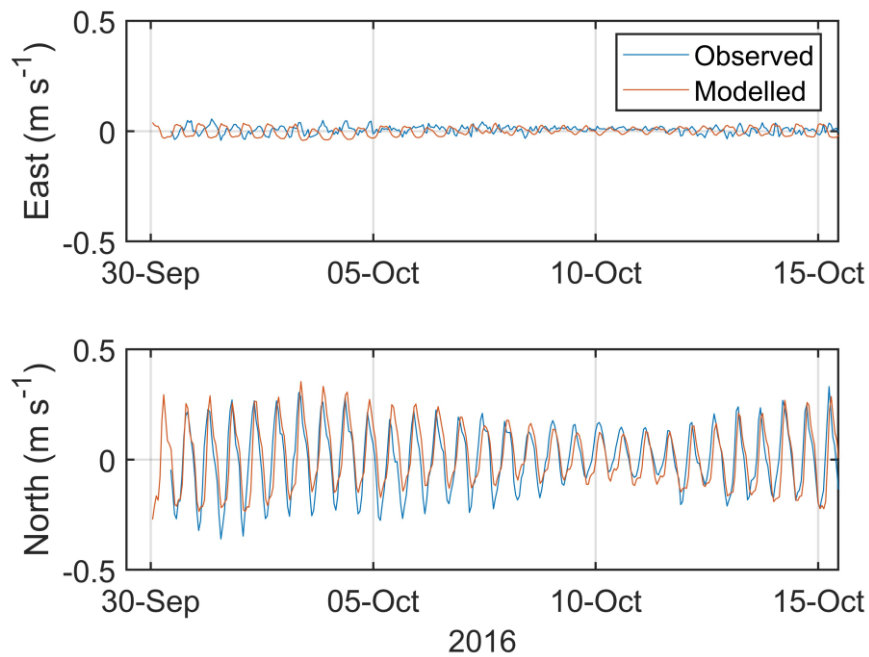


Figure 6. Comparison between observed and modelled East (top) and North (bottom) components of velocity at the ADCP location for 15 days in September - October 2018 (ID119). Observed data are in blue, model results in red.

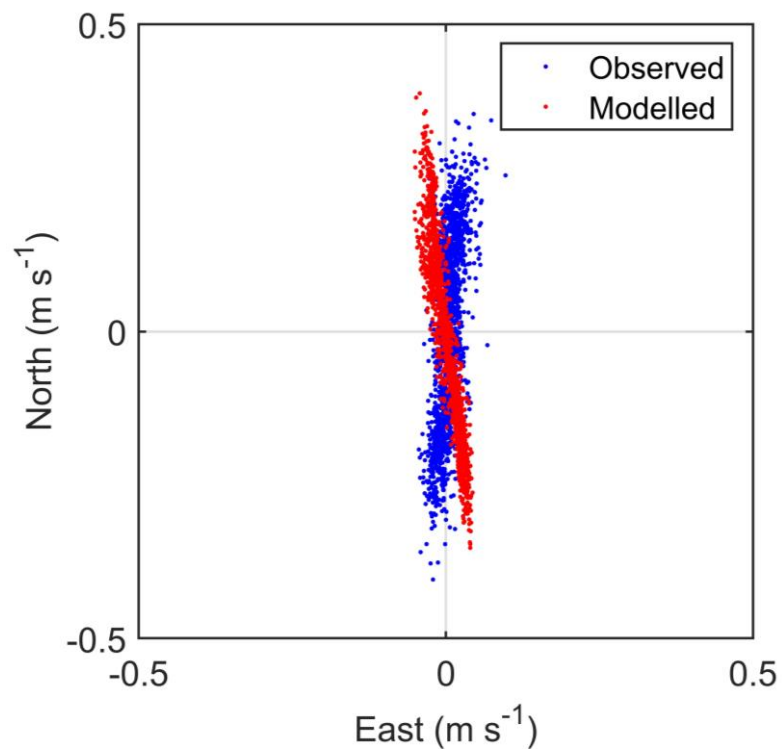


Figure 7. Scatter plot of observed and modelled velocity at the ADCP location from September - December 2016 (ID119). Observed data are in blue, model results in red.

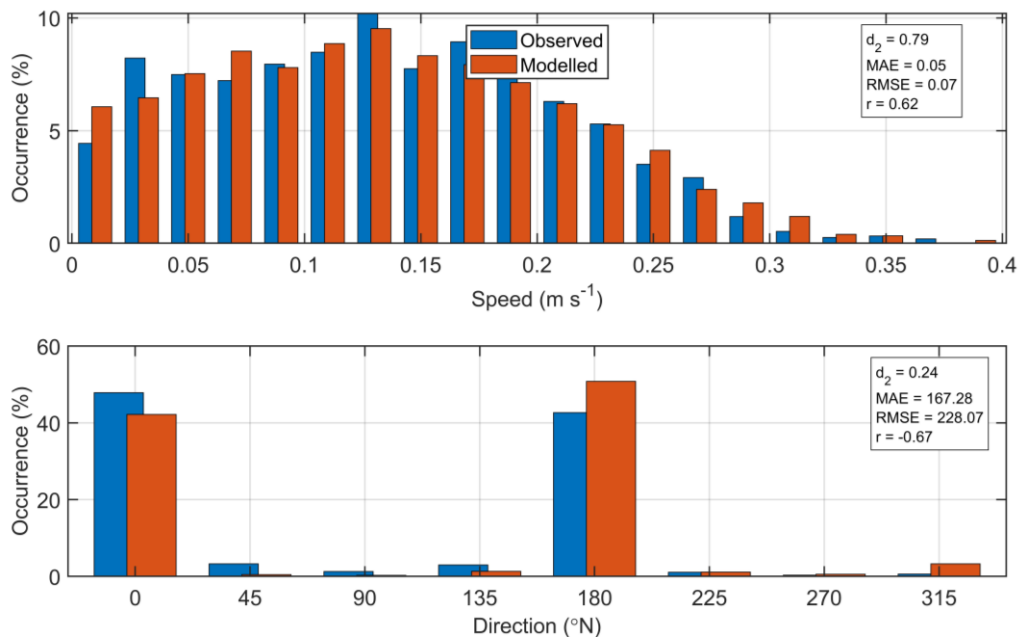


Figure 8. Histograms of observed and modelled speed (top) and direction (bottom) at the ADCP location from September – December 2016 (ID119). Observed data are in blue, model results in red.

### 3.2 Validation: August – October 2017, ID182

At the ADCP location, the sea surface height was accurately modelled, with model skill of 0.98 (Figure 9, Table 3). The mean absolute error (MAE) and root-mean-square error (RMSE) values of 0.19 m and 0.24 m are about 4.8 % and 6.0 % of the spring tide range (ca. 4 m) respectively.

East and North components of velocity at the ADCP location were satisfactorily reproduced by the model, with values of the model skill,  $d_2$ , of 0.12 and 0.93 respectively (Figure 10, Table 3). The values of the MAE and RMSE being in the range 0.02 – 0.08  $\text{m s}^{-1}$  (Table 3). The scatter plots and histograms shown in Figure 11 and Figure 12 demonstrate that the modelled currents were broadly of the same speed and direction as the observed data.

Table 3. Model performance statistics for sea surface height (SSH) and East and North velocity at the ADCP location from August – October 2017 (ID182).

	SSH	East	North
Skill, $d_2$	0.98	0.12	0.93
Mean Absolute Error (MAE)	0.19 m	0.02 $\text{m s}^{-1}$	0.07 $\text{m s}^{-1}$
Root-Mean-Square Error (RMSE)	0.24 m	0.03 $\text{m s}^{-1}$	0.08 $\text{m s}^{-1}$

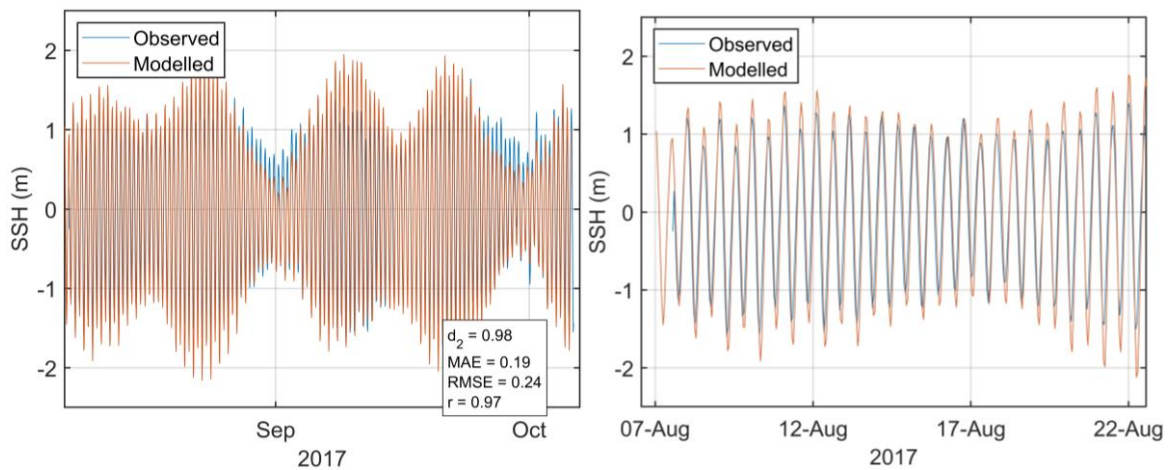


Figure 9. Comparison between observed and modelled sea surface height from August– October 2017 (ADCP deployment ID182) using model parameter values from Table 1. Both the full record (left) and a subset of 15 days (right) are shown. Observed data are in blue, model results in red.

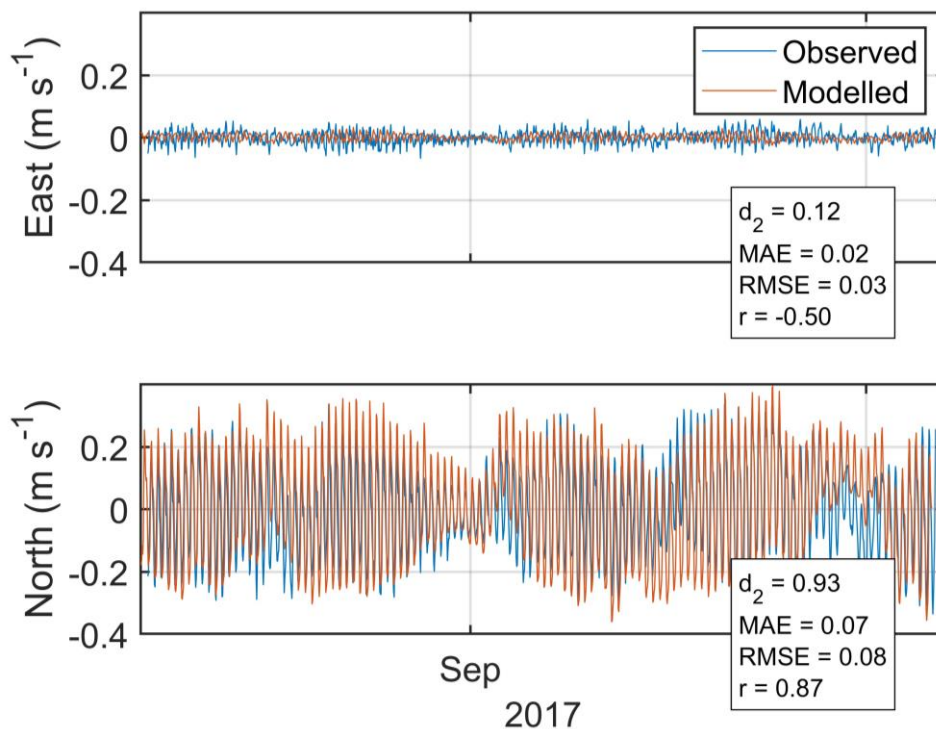


Figure 10. Comparison between observed and modelled East (top) and North (bottom) components of velocity at the ADCP location for 15 days in August – October 2017 (ID182). Observed data are in blue, model results in red.

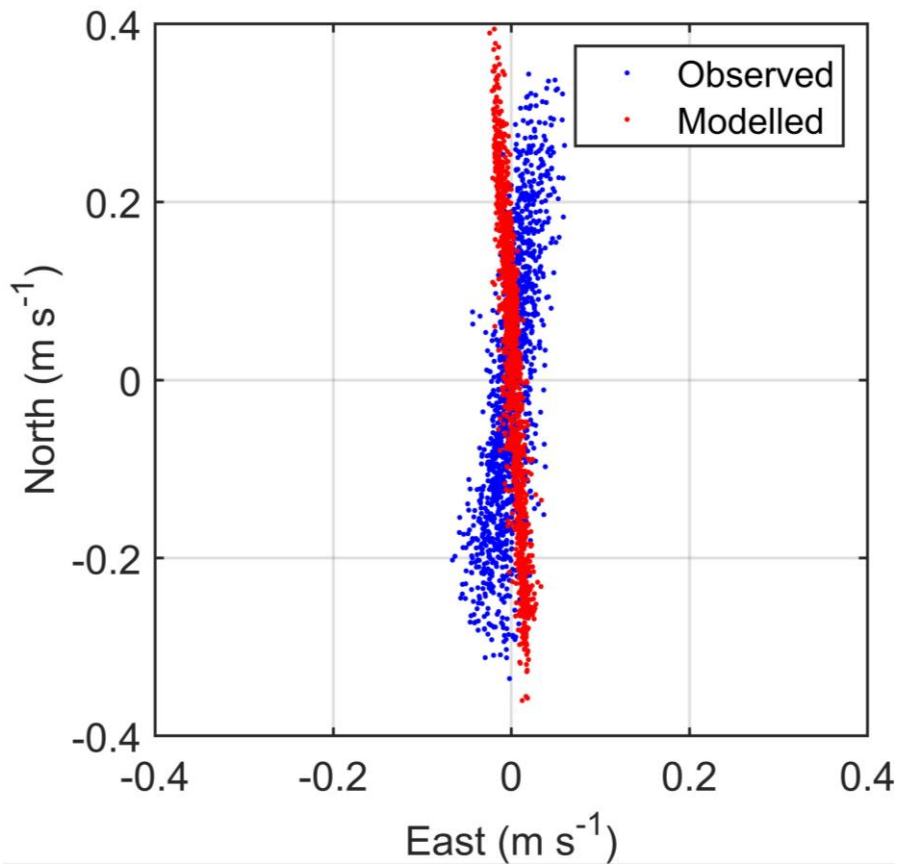


Figure 11. Scatter plot of observed and modelled velocity at the ADCP location from August – October 2017 (ID182). Observed data are in blue, model results in red.

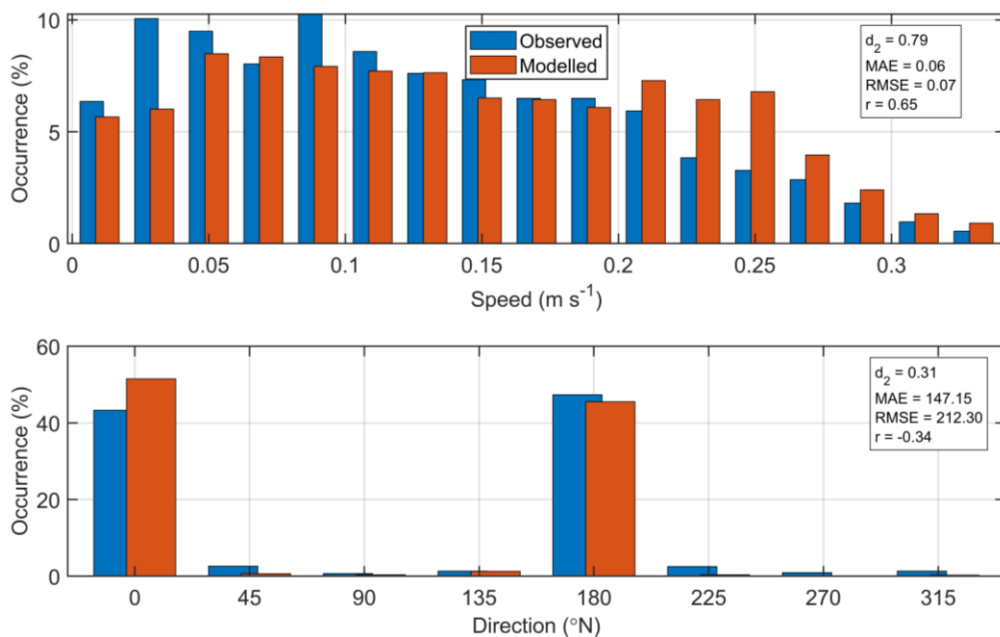


Figure 12. Histograms of observed and modelled current speed (top) and direction (bottom) at the ADCP location from August – October 2017 (ID182). Observed data are in blue, model results in red.

#### 4. Modelled Flow Fields (ID119)

Modelled flood and ebb velocity vectors at a spring tide on the 17<sup>th</sup> and 18<sup>th</sup> of October 2016 are illustrated in Figure 13. The Carradale sites are exposed to strong currents, with flood tide current speeds of up to  $44 \text{ cm s}^{-1}$ . Currents around the Carradale sites have a mean speed of  $0.14 \text{ m s}^{-1}$  and near-bed current speeds of  $0.12 \text{ m s}^{-1}$ .

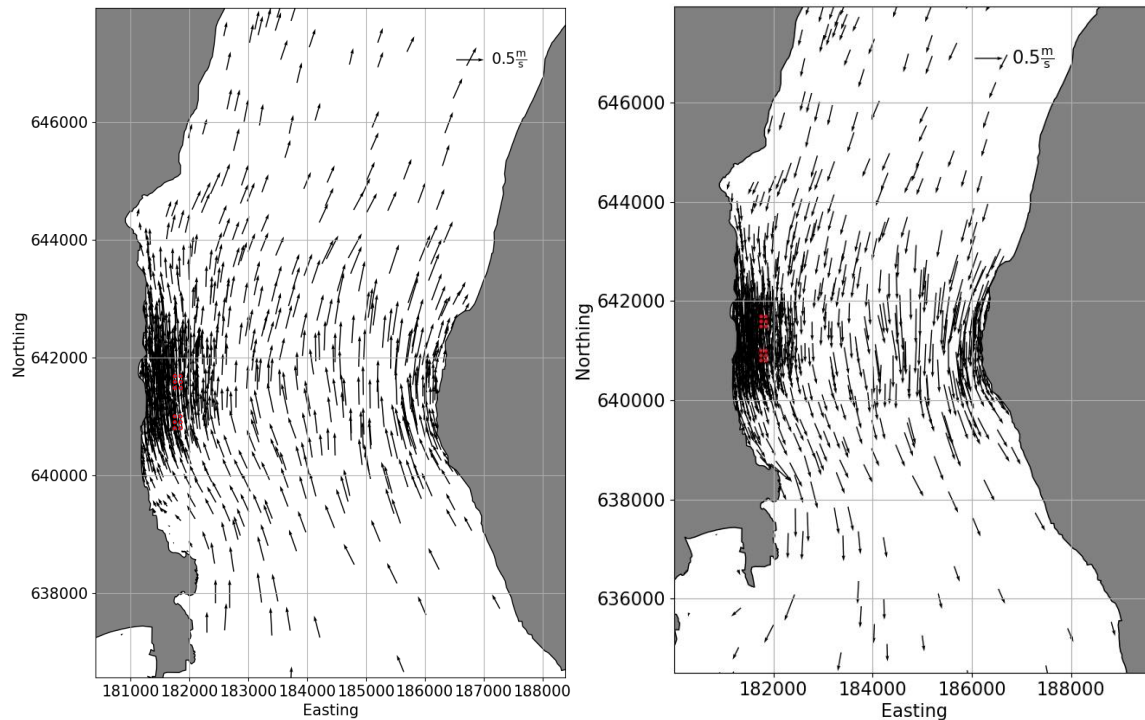


Figure 13. Modelled flood (left) and ebb (right) surface current vectors during spring tides. For clarity, only every 10<sup>th</sup> vector is shown.

#### 5. References and Bibliography

Casulli, V. 1987. Eulerian-lagrangian methods for hyperbolic and convection dominated parabolic problems. In: Taylor, C., Owen, D., Hinton, E. (Eds.), Computational Methods for Non-linear Problems, Pineridge Press, Swansea, U.K., pp. 239–268.

European Centre for Medium-Range Weather Forecasts (ECMWF) 2021, ERA5 Dataset <https://www.ecmwf.int/en/forecasts/datasets/reanalysis-datasets/era5>

Gillibrand, P.A.; Lane, E.M.; Walters, R.A.; Gorman, R.M. 2011. Forecasting extreme sea surface height and coastal inundation from tides, surge and wave setup. *Austr. J. Civil Eng.* 9, 99-112.



- Gillibrand, P.A., Walters, R.A., and McIlvenny, J., 2016. Numerical simulations of the effects of a tidal turbine array on near-bed velocity and local bed shear stress. *Energies*, vol 9, no. 10, pp. 852. DOI: 10.3390/en9100852
- Lane, E.M.; Gillibrand, P.A.; Arnold, J.R.; Walters, R.A. 2011. Tsunami inundation modelling with RiCOM. *Austr. J. Civil Eng.*, 9, 83-98.
- Large, W.G. and Pond, S., 1981. Open ocean momentum flux measurements in moderate to strong winds. *J. Phys. Oceanogr.*, 11, 324—336.
- Marine Scotland, 2016. The wider domain Scottish Shelf Model | Marine Scotland Information <https://marine.gov.scot/information/wider-domain-scottish-shelf-model>
- Marine Scotland, 2019. The Firth of Clyde Model | Marine Scotland Information <https://marine.gov.scot/information/firth-clyde-model>
- McIlvenny, J., Tamsett, D., Gillibrand, P.A. and Goddijn-Murphy, L., 2016. Sediment Dynamics in a Tidally Energetic Channel: The Inner Sound, Northern Scotland. *Journal of Marine Science and Engineering*, 4, 31; doi:10.3390/jmse4020031
- Mowi Scotland Ltd, 2023. Carradale Azamethiphos Dispersion Modelling Report. December 2023.
- Plew, D. R.; Stevens, C. L. 2013. Numerical modelling of the effect of turbines on currents in a tidal channel—Tory Channel, New Zealand. *Renew. Energy*, 57, 269-282.
- Walters, R. A. 2005a. Coastal ocean models: two useful finite element methods. *Cont. Shelf Res.*, 25(7), 775-793.
- Walters, R. A. 2005b. A semi-implicit finite element model for non-hydrostatic (dispersive) surface waves. *Int. J. Num. Meth. Fluids*, 49(7), 721-737.
- Walters, R.A. 2016. A coastal ocean model with subgrid approximation. *Ocean Mod.*, 102, 45-54.
- Walters, R.A.; Casulli, V., 1998. A robust, finite element model for hydrostatic surface water flows. *Comm. Num. Methods Eng.*, 14, 931–940.
- Walters, R.A.; Gillibrand, P.A.; Bell, R.; Lane, E.M. 2010. A Study of Tides and Currents in Cook Strait, New Zealand. *Ocean Dyn.*, 60, 1559-1580.
- Walters, R.A., Lane, E.M., Hanert, E. 2009. Useful time-stepping methods for the Coriolis term in a shallow water model. *Ocean Model.*, 28, 66–74. doi: 10.1016/j.ocemod.2008.10.004.
- Walters, R.A. ; Lane, E.M.; Henry, R.F. 2008. Semi-lagrangian methods for a finite element coastal ocean model. *Ocean Model.*, 19, 112–124.
- Walters, R. A.; Tarbotton, M. R.; Hiles, C. E. 2013. Estimation of tidal power potential. *Renew. Energy*, 51, 255-262.

Willmott, C. J.; Ackleson, S. G.; Davis, R. E.; Feddema, J. J.; Klink, K. M.; Legates, D. R. O'Donnell, J.; Rowe, C. M. 1985. Statistics for evaluation and comparison of models, *J. Geophys. Res.*, 90, 8995– 9005.

Wu, J. 1982. Wind-stress coefficients over sea surface from breeze to hurricane, *J. Geophys. Res.*, 87(C12), 9704–9706, doi:10.1029/JC087iC12p09704.